CHEMICAL PHYSICS

Improving potential energy surfaces using measured Feshbach resonance states

Karl P. Horn[1]†, Luis Itza Vazquez-Salazar[2]†, Christiane P. Koch[1], Markus Meuwly[2]*

The structure and dynamics of a molecular system is governed by its potential energy surface (PES), representing the total energy as a function of the nuclear coordinates. Obtaining accurate potential energy surfaces is limited by the exponential scaling of Hilbert space, restricting quantitative predictions of experimental observables from first principles to small molecules with just a few electrons. Here, we present an explicitly physics-informed approach for improving and assessing the quality of families of PESs by modifying them through linear coordinate transformations based on experimental data. We demonstrate this "morphing" of the PES for the He - H_2^+ complex using recent comprehensive Feshbach resonance (FR) measurements for reference PESs at three different levels of quantum chemistry. In all cases, the positions and intensities of peaks in the energy distributions are improved. We find these observables to be mainly sensitive to the long-range part of the PES.

INTRODUCTION

The potential energy surface (PES) representing the total energy of a molecule is a fundamental concept for characterizing the dynamics both in the gas and condensed phase (1, 2). With high-quality PESs, the computation of experimental observables becomes possible with predictive power at a quantitative level. On the other hand, while essential measurable observables such as reaction cross sections, thermal rates, or relaxation times directly depend on it, the PES itself cannot be observed. This raises the question of how to obtain the most accurate PES for a given system. From an electronic structure perspective, it is known that within the Born-Oppenheimer approximation and neglecting relativistic and quantum electrodynamic corrections (3) full configuration interaction (FCI) calculations with large basis sets provide the highest quality for the total energies of a molecule. However, the unfavorable scaling of FCI with the number of electrons and basis functions prevents its routine use for constructing full-dimensional PESs for any molecule consisting of more than a few light atoms. Alternatively, one may approach the question from an experimentalist's perspective and argue that the "most accurate PES" is the one that best describes physical observations. Such an approach has been developed for diatomic molecules: the rotational Rydberg-Klein-Rees (RKR) method solves the "inversion problem" of obtaining the potential energy curve given spectroscopic information (4). Rotational RKR has also been applied to triatomic van der Waals complexes (5, 6) but cannot be extended to molecules of arbitrary size. Solving the "inverse problem," i.e., determining the PES given experimental observables and an evolution equation from which these observables are calculated has in general turned out to be very difficult in chemical physics (7). This concerns both the choice of observables and the actual inversion procedure.

An alternative that is not particularly sensitive to the dimensionality of the problem is to reshape the PES which was first done by trial and error (8, 9) and eventually lead to "morphing" PESs (10). This method exploits the topological relationship between a reference and a target PES. Provided that calculations with the reference PES yield qualitatively correct observables $\mathcal{O}_{calc}$ when compared with experimental observations $\mathcal{O}_{exp}$, the squared difference $\mathcal{L} = |\mathcal{O}_{calc} - \mathcal{O}_{exp}|^2$ can be used to reshape the PES through linear or nonlinear coordinate transformations (morphing) (10). It capitalizes on the correct overall topology of the reference PES and transmutes it into a new PES by stretching or compressing internal coordinates and the energy scale, akin to stretching and bending a piece of rubber. Alternatives for reshaping PESs are machine learning-based methods such as Δ−ML (11), transfer learning (12, 13), or differential trajectory reweighting (14). Morphing has been applied successfully to problems in spectroscopy (15), state-to-state reaction cross sections (16), and reaction dynamics (17) for systems with up to 6 atoms (18). Near-quantitative, full-dimensional reference PESs from electronic structure calculations have, however, so far rarely been available for direct comparison. For scattering experiments with He − H_2^+ such a PES is now available (19). On the other hand, for weakly interacting triatomic van der Waals complexes, accurate PESs were determined from fitting well depths and positions of radial minima to parametrized functions (20). However, these studies relied heavily on explicitly available long-range information of the intermolecular interactions. The present work approaches the problem from a broader perspective, formulates and solves it as a machine learning-based task, and applies it to recently measured scattering data covering a wide range of intermolecular energies.

The He − H_2^+ molecular complex is an ideal proxy for the present work owing to the fact that the PES can be calculated rigorously at the highest level of quantum chemistry (FCI). The complex is also interesting in itself, and the current status of experimental and computational spectroscopy and reaction dynamics has recently been reviewed (21). He − H_2^+, which is isoelectronic to H_3, is stable in its electronic ground state and features a rich reaction dynamics and spectroscopy. Experimentally, near-dissociation states (22, 23) and the low-resolution spectroscopy were reported for both, He − H_2^+ and He − D_2^+ (24). Assignments of the vibrational bands were possible by comparing with bound state calculations using a FCI PES (19). Only recently, it was possible to estimate the dissociation energy of ∼1800 cm^{-1} from spectroscopic measurements (24). This compares with earlier bound state calculations using the FCI PES predicting a value of $D_0 = 1784$ cm^{-1} (19). This value was confirmed from a

[1]Dahlem Center for Complex Quantum Systems and Fachbereich Physik, Freie Universität Berlin, Arnimallee 14, D-14195 Berlin, Germany. [2]Department of Chemistry, University of Basel, Klingelbergstrasse 80, CH-4056 Basel, Switzerland.
*Corresponding author. Email: m.meuwly@unibas.ch
†These authors contributed equally to this work.

subsequent focal point analysis resulting in $D_0 = 1789(4)$ cm^{-1} for para $- H_2^+$ (25). Furthermore, a range of reactive collision experiments was carried out which yielded total and differential cross sections, depending on the vibrational state of the diatomic (21) but with marked differences between observed and computed results. In particular, computationally predicted sharp reactive scattering resonances have not been found experimentally as of now (21). The role of nonadiabatic couplings is of considerable current interest as a means to clarify the role of geometric phase in reaction outcomes and as a source of friction in the formation of the He $- H_2^+$ complex in the early universe. This provides additional impetus for a comprehensive characterization of this seemingly "simple" system.

The present work uses all very high-quality experimentally measured (26) Feshbach resonances for He $- H_2^+$ to morph PESs. Feshbach(-Fano) resonances arise if a bound molecular state on a PES of a closed channel couples to scattering states in an open channel (27, 28). The recoil translational energy is determined from measurements which are expected to probe large spatial areas of a PES and the underlying intermolecular interactions (28). The redistribution of energy due to the Feshbach resonances has recently been mapped out comprehensively for He $- H_2^+$ and Ne $- H_2^+$ with coincidence velocity map imaging of electrons and cations, yielding very favorable agreement between theory and experiment (26). In these experiments, the ionic molecular complexes are generated at separations of up to 10 a_0 between the rare gas atom and the molecular ion, confirming that the experiment indeed probes a large spatial extent of the PES, including its long-range part.

Here, morphing is applied to initial PESs ranging from essentially exact FCI (apart from non–Born-Oppenheimer, relativistic, quantum electrodynamic, and remaining basis set effects) to medium- and lower-level methods, that is, multireference configuration interaction including the Davidson correction (MRCI + Q) and second-order Møller-Plesset perturbation theory (MP2). This allows determining the sensitivity of the PES and information content in the experimental observables about local and global features of the PES and to assess the performance of lower-level methods (e.g., MP2) compared with FCI. Starting from a PES of sufficiently high quality, the changes introduced by morphing can be related to parts of the PES that are probed by the experiments. At the same time, additional experimental observables, probing primarily the bound region for He interacting with H_2^+, will be required for morphing at the lower levels of quantum chemical theory.

RESULTS

The three PESs considered in the present work, in decreasing order of rigor, were determined at the FCI, MRCI + Q, and MP2 levels of theory, using Jacobi coordinates R (distance between the center of mass of the H_2^+ and He), r (distance between the two hydrogen atoms), and θ (the angle between the two vectors $\vec{R}$ and $\vec{r}$), see Fig. 1A. To set the stage, scattering calculations with the FCI PES are considered which give quite satisfactory results when compared with the experimental data (Fig. 2A and Table 1). The measured kinetic energy distributions feature a series of peaks which reflect the rovibrational quenching associated with the decay of the Feshbach resonances (26). On average, the positions of the peak maxima are reproduced to within 10.8 cm^{-1}, whereas the maximum intensities, I_{max}, of $P(E)$ differ by 20.9 arbitrary units (a.u.; blue squares in Fig. 2A).

Next, morphing was applied to all three PESs, including the FCI PES. The FCI PES has been validated with respect to experiment (22–24, 26) and therefore can serve as a suitable proxy for changes required for PESs at the MRCI + Q and MP2 levels of theory. Two morphing strategies were considered (Fig. 1B): For morphing M1, the total energy was decomposed into one-body ($\mathscr{V}_i^{(1)}$), two-body ($\mathscr{V}_i^{(2)}$), and three-body ($\mathscr{V}^{(3)}$) contributions

$$V(R, r, \theta) = \mathscr{V}_{He}^{(1)} + \mathscr{V}_{H}^{(1)} + \mathscr{V}_{H+}^{(1)} + \\ \mathscr{V}_{HeH}^{(2)}(r_{HeH}) + \mathscr{V}_{HeH+}^{(2)}(r_{HeH+}) + \mathscr{V}_{H_2^+}^{(2)}(r_{H_2^+}) + \mathscr{V}^{(3)}(R, r, \theta) \quad (1)$$

and the morphing transformation was applied only to $\mathscr{V}^{(3)}(R, r, \theta)$. It should be noted that $\mathscr{V}^{(3)}(R, r, \theta)$ is defined as the difference between the total energy and the one- and two-body terms without implying a physical origin of the three-body contribution, such as an Axilrod-Teller interaction. Approach M1 is motivated by the assumption that all diatomic potentials $\mathscr{V}_i^{(2)}$ are of high quality so that changes are only required in the higher-order correction three-body term. In the second approach, called "M2," the PES is globally modified, including the two-body contributions. In other words, for M1 and M2, the morphing transformation (Eq. 4) is applied to $\mathscr{V}^{(3)}(R, r, \theta)$ and to $\mathscr{V}(R, r, \theta)$, respectively. The reduction of the total loss and the associated parameter values are reported in figs. S1 and S2.

Morphing M1 applied to the FCI PES leaves most of the peak positions unchanged, see filled versus open blue symbols in Fig. 2D, but improves the peak heights considerably (by 30%) as demonstrated in Fig. 2E and Table 1 (rightmost column). These improvements are accommodated by reshaping the underlying PES as shown in Fig. 3A: In the long-range ($R > 3.0$ a_0), the anisotropy of the morphed FCI-PES is somewhat decreased due to reshaping the PES around $\theta = 90°$ (T-shaped geometry) and D_e is decreased by ~50 cm^{-1}. One-dimensional (1D) cuts along the r_{HH} and R coordinates for a given angle θ show that changes in the PES become more substantial for larger r_{HH} with small changes in the depth of the potential wells but maintaining the overall shape (figs. S3 and S4). The changes with respect to R are noticeable for $R < 3.0$ a_0 with distortions of the energy contours at different angles θ but maintaining the overall shape of the curves. For increasing R, the changes are negligible compared with the original PES, reflecting the accurate treatment of the long-range interaction (fig. S3). 2D projections of the combined changes of r_{HH} and R at different angles show that the most pronounced modifications in the shape of the PES concern regions for r_{HH} larger than the equilibrium geometry of H_2^+ (figs. S5A, S6A, and S7A).

FCI calculations of entire PESs with sufficiently large basis sets are only feasible for few-electron systems. For larger systems, quantum chemical methods such as Møller-Plesset perturbation theory, multireference configuration interaction, or coupled cluster-based techniques need to be used instead. As reported in the two rightmost columns of Table 1, the initial MRCI + Q and MP2 PESs reproduce experimental peak positions within 10.3 and 13.1 cm^{-1} compared with 10.8 cm^{-1} from the FCI PES, and for the peak intensities, the and root mean squared errors (RMSEs) are 23.9 and 22.4 compared with 20.9 a.u. from using the highest level of electronic structure theory. On the other hand, the dissociation energy is smaller by more than 10% compared with the FCI PES due to partial neglect of correlation energy in the MRCI + Q and MP2 methods. This confirms that Feshbach resonances are not particularly informative with regard to features of the PES around the minimum energy structure ($R \sim 3.0$ a_0),
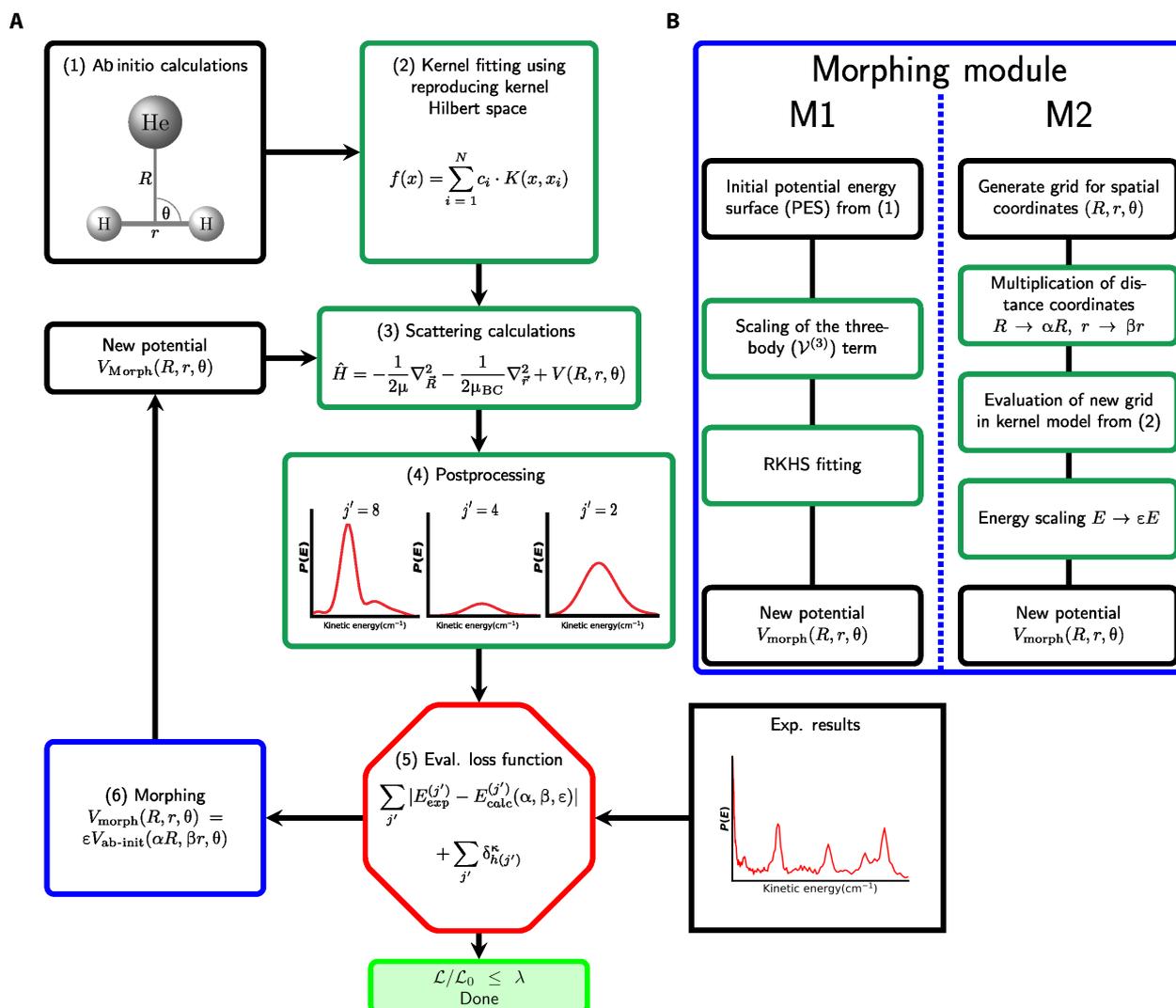
Fig. 1. Morphing of ab initio potentials based on experimental data. General flowchart of the morphing procedure (**A**): Module (1) implements the calculation of ab initio points for the system under study, the triatomic $He - H_2^+$ with the definition of the respective coordinates indicated. Module (2) represents the fitting of the points obtained from the previous step using the reproducing kernel Hilbert space (RKHS) method, with the functional form used to approximate the given PES. Module (3) corresponds to the scattering calculations performed with the potential obtained in module (2), calculating the eigenstates of the Hamiltonian. Module (4) postprocesses the results of the scattering calculations to yield $P(E)$ with examples for three values of j' displayed. Module (5) evaluates the loss function (Eq. 5) for morphing, comparing the experimental values of the energy distributions with the results of the scattering calculations. Module (6) carries out the actual morphing procedure, as explained in (B). Morphing results in a new potential, and the procedure continues until the value of the loss function in module (5) does not improve further. The termination conditions are $\mathscr{L}/\mathscr{L}_0 \leq \lambda_{M1} = 0.3$ or $\mathscr{L}/\mathscr{L}_0 \leq \lambda_{M2} = 0.4$ for M1 and M2, respectively where $\mathscr{L}_0$ is the loss function of the unmorphed energy distribution, see fig. S1. (**B**) Morphing module (6) for procedures M1 (three-body) and M2 (global).

although the wave functions sample this region extensively, see fig. S8. In other words, although an important characteristic of a PES such as the stabilization energy of the complex differs by 10% or more, the energies and intensities measured in collision experiments are matched within similar bounds.

Morphing M1 applied to the MRCI + Q and MP2 PESs supports this observation. The loss function evaluated in module (5) of the optimization, see Fig. 1, decreased by 74 and 88% for the two cases, with improvements in the intensities by up to 50% for the MP2 PES, see Table 1 (far right column). However, the resulting PESs are clearly unphysical, with pronounced distortions in particular for the MP2

PES (see Fig. 3C), and dissociation energies either increased by 40% for MRCI + Q or decreased by 30% for MP2, respectively. Low-resolution experiments (*24*) provide an estimate for the dissociation energy $D_0 \sim 1800$ cm^{-1}, compared with $D_0 = 1794$ cm^{-1} from bound state calculations on the initial FCI PES (*19*) which features a well depth of $D_e \sim 2820$ cm^{-1}. This value of D_e serves as a reference for the remainder of the present work.

The percentage changes of the parameters [α, β, ε] scaling (R, r, V) provide further information about the transformation induced by morphing the initial PESs. For the FCI PES, they are (−0.6, −3.6, 0.0)% compared with (−0.6, 11.6, 1.0)% for the MRCI + Q and
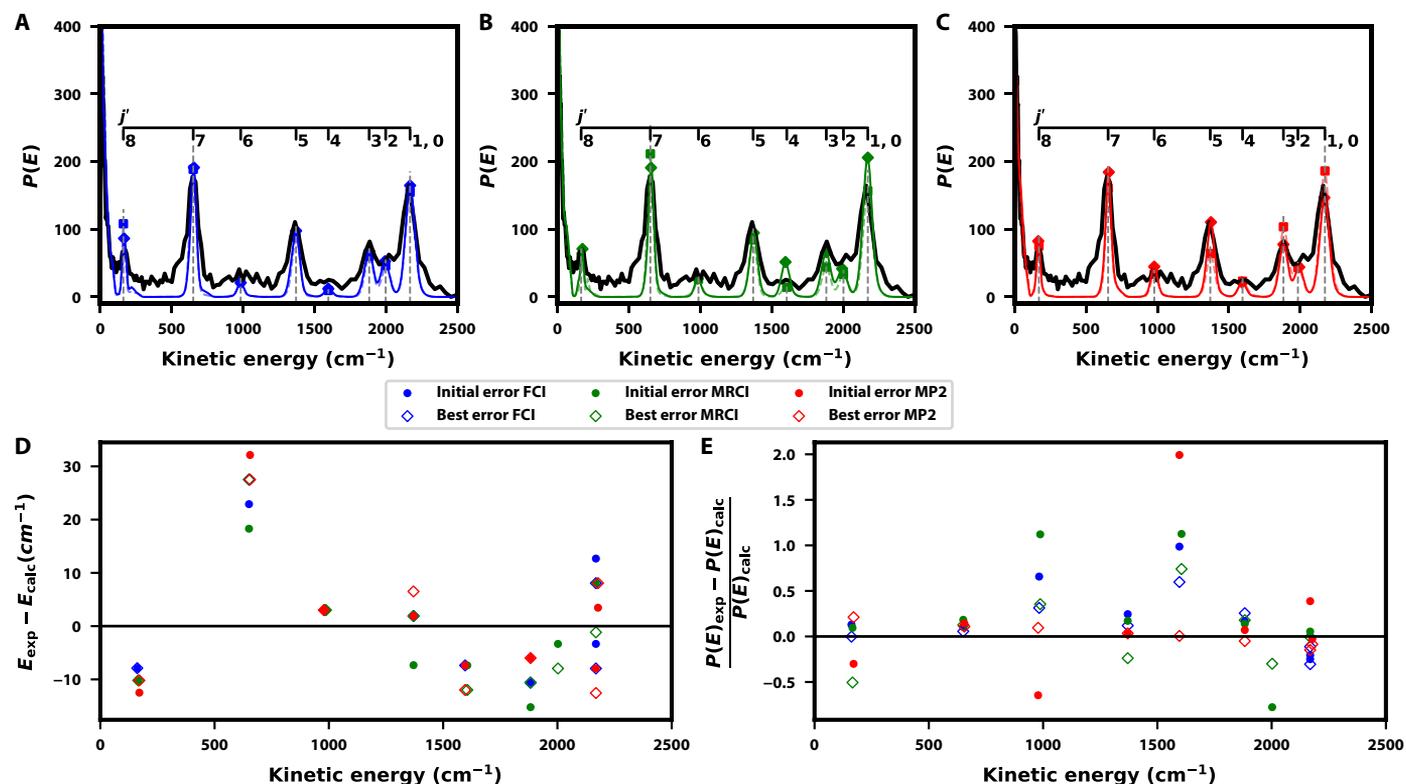
Fig. 2. Comparison of calculated energy distributions P(E) from unmorphed and morphing M1 PESs with experimental results. $P(E)$ obtained from experiment [black, data taken from (*26*)] and full coupled channels calculations using the unmorphed and M1-morphed PESs for FCI (**A**), MRCI + Q (**B**), and MP2 (**C**). Computed results for the initial (blue, green, and red dashed) and best (blue, green, and red solid) morphed PESs are reported, with the residuals for the peak positions ($E_{exp} - E_{calc}$) and fraction of error in the peak heights $\left[\left(\frac{P(E)_{exp} - P(E)_{calc}}{P(E)_{calc}}\right)\right]$ for each PES shown in (**D**) and (**E**). The statistical measures for all models are summarized in Table 1. The experimental uncertainties are 3.5 cm^{-1} for the peak positions and ~10% for peak heights.

Table 1. Dissociation energies (D_e in cm^{-1}) for He + H$_2^+$, coordinates for the minimum energy structures, R_e and r_e, and root mean squared errors (RMSEs) for the peak positions and heights of the kinetic energy spectra for all initial and morphed PESs using both M1 and M2 methods. In all cases, the equilibrium geometry is linear He − H$_2^+$, i.e., $\theta = 0$ or $\theta = 180°$.

Surface	D_e (cm^{-1})	R_e/a_0	r_e/a_0	RMSE (E) (cm^{-1})	RMSE (I) (a.u.)
FCI initial	2818.9	2.97	2.07	10.8	20.9
FCI morphed (M1)	2772.0	2.95	2.07	11.9	13.7
FCI morphed (M2)	2819.1	2.99	2.07	10.8	13.8
MRCI + Q initial	2557.3	2.98	2.07	10.3	23.9
MRCI + Q morphed (M1)	3414.7	2.98	2.08	12.2	21.9
MRCI + Q morphed (M2)	2557.0	3.00	2.03	8.9	17.6
MP2 initial	2494.0	2.99	2.07	13.1	22.4
MP2 morphed (M1)	1685.6	2.93	2.12	12.8	10.9
MP2 morphed (M2)	2492.8	2.97	1.74	10.0	11.8
MP2 morphed (PES to PES)	2502.3	2.98	2.06	13.0(7)	22.9

(0.3, −9.7, 0.1)% for the MP2 PES. The most notable changes concern the H$_2^+$ vibrational coordinate r_{HH} for MRCI + Q (+12.0%) and MP2 (−10.0%). Such large changes are problematic since the many-body expansion used for morphing M1, cf. Eq. 1, relies on the quality of the two-body contributions, i.e., the H$_2^+$ and HeH$^+$ potential energy curves. However, MP2 underestimates the experimentally determined

dissociation energy of the HeH$^+$ two-body interaction by 285 cm^{-1} (fig. S9) and accounts for an overall error of ~500 cm^{-1} in D_e for He − H$_2^+$. On the other hand, the two-body term for H$_2^+$ agrees to within 3 cm^{-1} between the three methods with remaining differences compared with experiment primarily due to neglect of non–Born-Oppenheimer contributions (fig. S10), relativistic corrections, quantum
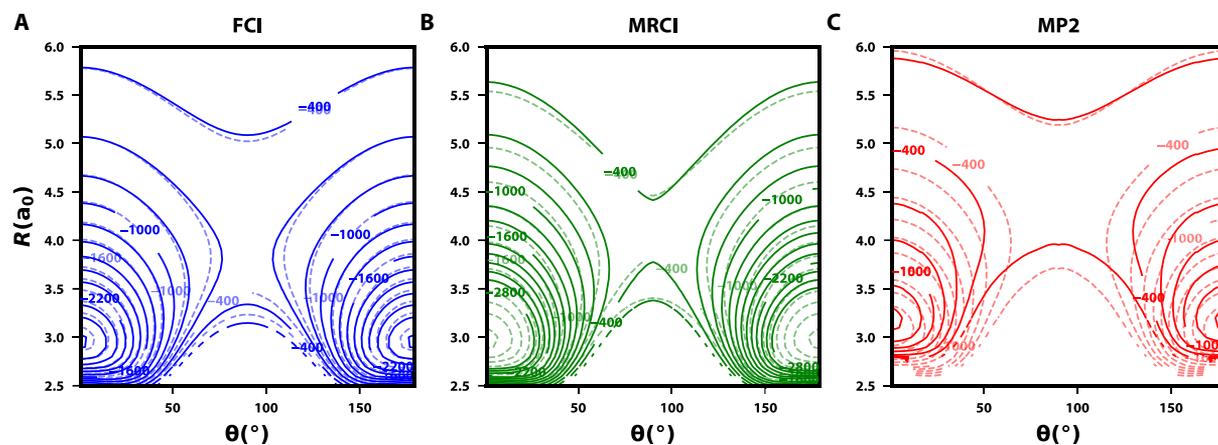
Fig. 3. Comparison between unmorphed and morphed M1 PESs. Projections of the PESs for $r_{HH} = 2.0$ a_0 for the three methods studied here. Isocontours for unmorphed PESs [FCI (**A**, blue), MRCI + Q (**B**, green), and MP2 (**C**, red) from left to right] are shown as dashed lines, whereas the M1-morphed PESs are solid lines. The zero of energy is set by the value at $r = 2.0$ a_0 and $R = \infty$. Energies are in cm^{-1}.

electrodynamic effects, and remaining basis set incompleteness. To summarize, while M1 morphing improves the match between experimentally measured and calculated observables, it modifies the PES for the lower-level methods in an unphysical way. This is attributed to the fact that M1 morphing operates on the three-body term only and can thus not compensate for inaccuracies in the two-body contributions to the overall PES. In contrast, for FCI, the changes for all characteristics of the morphed PES are moderate, underscoring the accuracy of both, the initial and morphed PESs from FCI calculations.

To reduce the dependence of the morphed PESs on the quality of the two-body contributions, morphing M2 was carried out. M2 morphing acts globally and independently on each of the internal degrees of freedom, see Fig. 1. This makes M2 less prone to overcompensatory effects as observed for M1 morphing. For the MRCI + Q PES, the improvement in the observables amounts to ≈14% for the peak positions and ≈26% for the peak heights. At the same time, the changes in the PES are moderate, see Fig. 4B, and the dissociation energy does not change (Table 1) although the energy scaling parameter, ε, was allowed to vary. Similarly, for MP2, the RMSE for the positions and heights of the peaks improve by about 22 and 47%, respectively. Contrary to M1, morphing M2 does not substantially modify the well depth as reflected by the value of D_e, see Table 1. For FCI, morphing changes D_e by 0.2 cm^{-1}, which is plausible as increasing the basis set from aug-cc-pv4z to aug-cc-pv5z changes D_e by 5 cm^{-1} (fig. S11) and expected smaller changes when further increasing to the aug-cc-pv6z basis. This is confirmed for MRCI + Q calculations for which D_e changes by 2.5 cm^{-1} between aug-cc-pv5z and aug-cc-pv6z bases, see fig. S12.

For the optimal morphing parameters, M2 applied to the MRCI + Q PES yields an enlargement of R by ~1%, whereas r_{HH} is reduced by 1.9% and ε remains unaffected. The reduction in r_{HH} leads to a small increase in the height of the barrier between the two wells of the potential (Fig. 4B) and a corresponding increase in the energy of the transition state, as observed in the minimum energy path (MEP), see fig. S13, for the angular coordinate. This effect is compensated by a positive displacement of the values of R (fig. S14) for the MEP. On the other hand, for the MP2 surface, the morphing parameters are (+0.6, +19.0, −0.04)%. The large positive value for β results in a

displacement of the H_2^+ bond length to a shorter equilibrium value (figs. S15 and S16). For the R coordinate, the values are also reduced, while the barrier height remains unchanged (fig. S14). As for M1, in the MP2 and MRCI + Q PESs, the largest changes are observed in the r_{HH} coordinate. However, in the M2 method, scaling of the global PES results in a better performance for the calculation of the observable and a better physical description.

Morphing one PES into another one can probe the flexibility of the morphing transformation as a whole. To this end, the MP2 PES was morphed to best compare with the FCI PES in a least squares sense according to method M2, i.e., by finding parameters (α, β, ε) that minimize $(V_{FCI}(R, r, \theta) - \varepsilon V_{MP2}(\alpha R, \beta r, \theta))^2$ without specifically weighting low- or high-energy regions in the fit. In this case, no experimental data were used in the refinement. Rather, the performance of the morphed PES was tested a posteriori. This optimization procedure reduces the RMSE between the FCI and unmorphed versus morphed PES by about 30% (from 138 to 87 cm^{-1}; see fig. S17). The changes in the topology of the surface in Fig. 5C indicate that the morphed MP2 PES is "pulled toward" the FCI PES: Consider, for example, the isocontours for −400 cm^{-1} for which the original MP2 isocontour (blue) is far away from the FCI target contour (red), whereas the morphed PES (gray) is deformed toward the gray target isocontour. Closer inspection reveals this to occur for all the other isocontours in Fig. 5C as well. The barrier separating the $[He-HH]^+$ and $[HH-He]^+$ minima is reduced, which is also seen in the MEP (see fig. S18).

The results of the scattering calculations performed with the surface from the PES-to-PES morphing procedure (Fig. 5A) are overall slightly inferior to those obtained from the initial FCI and MP2 PESs, when compared with the experimental data: A negligible increase of the RMSE for the peak positions (<1%) and intensities (2.2%) is found. Moreover, the fact that the morphing transformation increases the well depth by merely 10 cm^{-1} indicates that a morphing transformation operating only on distances and the energy is not sufficiently flexible to accommodate global changes between topologies as different as FCI versus MP2. Some further improvement may be obtained by more heavily weighting data points in the attractive region compared with the repulsive well which was, however, not considered in the present work.
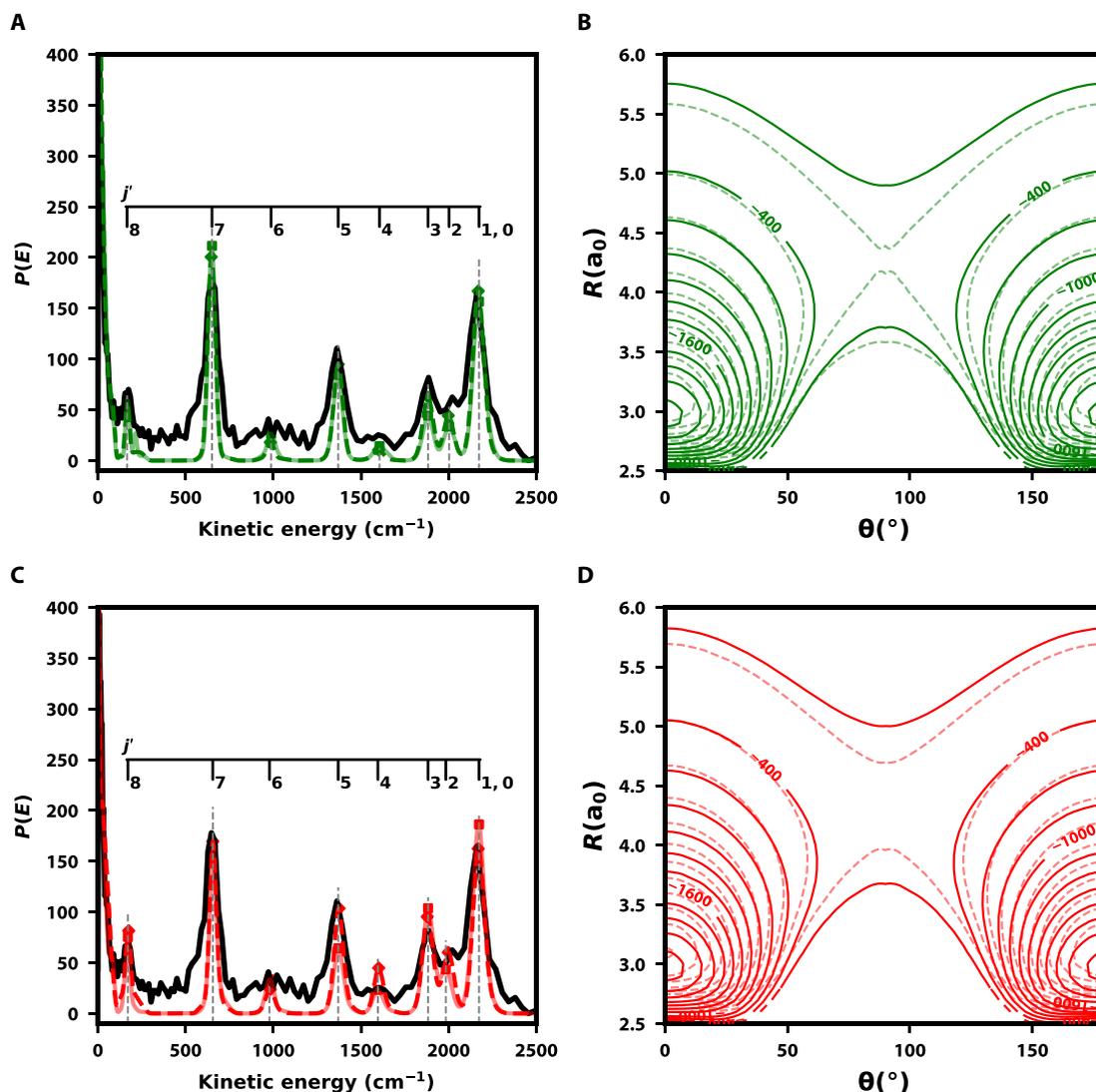
Fig. 4. Results of morphing method M2. Distributions $P(E)$ (**A** and **C**) obtained from experiment [black, data taken from (*26*)] and full coupled channels calculations using the unmorphed (dashed lines) and M2-morphed (solid lines) PESs (B and D) for MRCI + Q (A and B), and MP2 (C and D). The RMSE for the peak positions and heights are reported in Table 1. The projections of the PES (**B** and **D**) are shown for $r = r_e$ (see Table 1) with the zero of energy set for the r value considered and $R = \infty$. Energies are in cm^{-1}. The changes in the PES suggest that the observables are primarily sensitive to the long-range part and the repulsive wall of the PES.

The results indicate that at all levels of theory improvements in describing the experimental observables are possible. At the same time, morphing applied in the fashion done here provides a stringent test to probe the quality of an initial PES at a quantitative level—with higher initial levels of theory, the changes that need to be accommodated decrease and specific deficiencies of a particular quantum chemical approach can be unveiled.

DISCUSSION
Given that essentially exact quantum calculations are possible for the $He - H_2^+$ complex (*19*, *24*, *26*), the present results highlight what can and cannot be learned about molecular PESs—the central concept in classical and quantum molecular dynamics—from accurate and rather comprehensive experimental data based on Feshbach resonances.

One hallmark of such quantum scattering resonances is the large spatial extent of the PES which the resonance wave function probes (fig. S8 and discussion in the Supplementary Materials). In this regard, the kinetic energy spectrum obtained from the decay of the Feshbach resonances differs from spectroscopic observables, typically involving bound states sensitive to restricted spatial regions of the PES (*10*).

In addition to the actual changes of the PES, a comparison of the two morphing procedures used provides insight into the relationship between the PES, the information provided by specific observables, and how this information can be used to improve an initial PES. First, the much better performance of morphing the global interaction energy instead of restricting to the three-body contributions reveals the importance of corrections already at the level of two-body interactions. Moreover, the physically meaningful changes to the PES
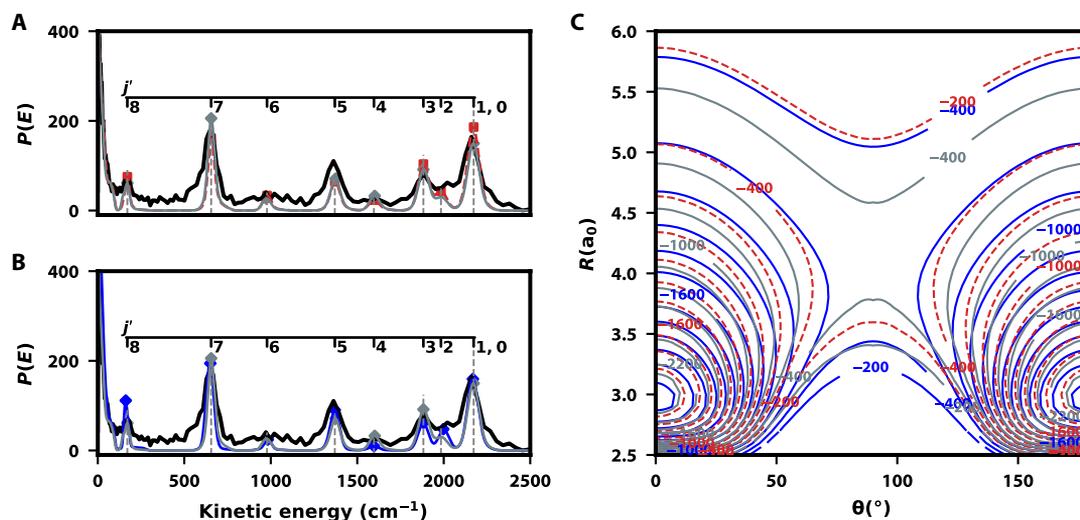
Fig. 5. PES-to-PES morphing. (**A**) Cross sections obtained from experiments [black, data taken from (26)] and scattering calculations on the unmorphed MP2 (dashed light red) and the morphed (gray) PESs for M2 PES-to-PES morphing procedure with the FCI PES as target. (**B**) Same as (A) but comparing the best morphed PES (gray) to the unmorphed FCI surface (solid blue). (**C**) 2D projections of the PES for $r = 2.0$ a_0 for unmorphed FCI (solid blue), unmorphed MP2 (dashed light red), and best-morphed PES (gray). The zero of energy is set to the value of the PES at $r_{HH} = 2.0$ a_0 and $R = \infty$. Energies are in cm^{-1}. All data points are equally weighted; the performance of the morphing transformation may be changed by differentially weighting attractive and repulsive regions of the PES.

identified by the global morphing concern essentially the anisotropy in the long range. To this end, comparatively small changes of the PESs result in notable improvements in the agreement between calculated and measured observables. This is in line with the expectation that Feshbach resonance wave functions mainly probe the anisotropy of the PES in the long range. Both observations taken together suggest extending the morphing transformation to include higher order terms (e.g., $\alpha r \rightarrow \alpha_1 r + \alpha_2 r^2 + \cdots$) or nonlinear terms (akin to a neural network activation function) in the coordinate transformation. Including the angular degree of freedom θ in the morphing transformation as well yields further improvements, see figs. S19 to S21 and discussion in the Supplementary Materials.

The present work provides information about the behavior of molecular PESs from lower (MP2) to very high (FCI) levels under morphing. It would also be interesting to characterize the effect of using different basis sets in the quantum chemical calculations. As an example, MRCI + Q calculations using the aug-cc-pV5z and aug-cc-pV6z basis sets changes the interaction energy between He and H_2^+ by 2.5 cm^{-1}, see fig. S12, compared with a well depth $D_e = 2557$ cm^{-1}. Hence, for the basis sets used in the present work, the effect is expected to be small. However, if smaller basis sets need to be used, as will be the case for larger systems, the effect will be considerably larger.

It is valuable to juxtapose the present effort to improve molecular PESs using experimental data with earlier work on van der Waals complexes between rare gas atoms and diatomic molecules. This approach was based on heavily parametrized functions including detailed expressions for the long-range part of the intermolecular interactions in which primarily the well depths and positions of the minima of the radial strength functions and the steepness of the repulsive wall were allowed to vary (20, 29). Such a strategy was successful in fine-tuning PESs but also relied on an appreciable amount of detailed information: For example, more than 20 parameters are required to define the long range interaction between the rare gas and

the diatomic molecule. In addition, uncertainties in the parameter values provided information about their sensitivity to experimental observables.

Contrary to this, the present work adopts a more holistic approach that also scales well to larger systems by deforming the entire PES to embed experimental observables. No particular physical meaning is attributed to the morphing parameters, and reporting uncertainties on them is of less immediate interest also because it is evident that multiple valid and meaningful solutions to the problem exist in general. At a more qualitative level, it is expected that the uncertainty on the well depths is appreciable because the experiments are not directly sensitive to this feature of the PES. The technique capitalizes on the fact that full-dimensional, global PESs can now be computed at sufficiently high levels of quantum chemistry (13), and obtaining a flexible machine learning-based rendering either from (reproducing) kernel representations or from neural networks is feasible (30, 31). The approach followed here can be easily scaled to larger systems, whereas the earlier "fine-tuning" strategies are typically limited to small systems. The present work extends the morphing methodology beyond spectroscopic observables to using experimental scattering cross sections. In the future, it will be interesting to combine observables whose dynamics are sensitive to different parts of the PES: sampling wide areas of configurational space (e.g., Feshbach resonances), state-to-state properties probing narrow ranges of the PES, such as spectroscopic transitions in the well, and near-dissociation states probing the high-energy regions of the well, to name a few.

At a fundamental level, the present findings raise the question how much and what experimental data are required to completely characterize a molecular PES. The present work proposes several PESs with comparable average performance on the scattering observables, although the shapes and local characteristics of the PESs differ greatly, illustrating that the information contained in the Feshbach resonances is not sufficient to uniquely define the PES. In particular, information on the bound-state region is missing. One possible way to answer

the question which combination of observables is suited to completely characterize the dynamics of a molecular system has been developed in quantum information science and is referred to as quantum process tomography (32). This has to be distinguished from the "tomography of Feshbach resonance states" (26) which referred to the simultaneous measurement of multiple reaction products. Quantum process tomography goes substantially further by providing a mathematical prescription to completely characterize a quantum dynamical process. It has been adapted to molecular systems, for example, in the context of ultrafast spectroscopy. It is, however, still an open question how to adapt it to two- or many-body processes such as molecular scattering. In future work, quantum process tomography could be applied to the quest of uniquely defining a PES by making use of the mapping between the real-space representation of the molecular Hamiltonian and qubits (33). This should allow for a systematic approach to identify the most important measurements which would then provide additional data for morphing PES.

METHODS

Potential energy surfaces

For the present work, three PESs were used. Full-dimensional PESs for $He − H_2^+$ were previously determined at the FCI/aug-cc-pV5Z and MRCI + Q/aug-cc-pV6Z levels of theory, respectively (19). The reference data were represented as a reproducing kernel Hilbert space (RKHS) (34, 35), which provides a highly accurate interpolation and allows to encode the leading order long-range behavior for large separations. In addition, a third PES using the same underlying grid for determining reference energies at the MP2/aug-cc-pV5Z level and also represented as a RKHS was constructed for the present work. These calculations were carried out using the MOLPRO suite of codes (36). All PESs are represented as a sum of diatomic potential energy curves together with an explicit three-body interaction. The complete many-body expansion for the $He − H_2^+$ system is given in Eq. 1, where distances $r_i \in \{r_{HeH}, r_{HeH+}, r_{H_2^+}\}$ in the two-body terms $\mathscr{V}_i^{(2)}$ are the distances between the respective atoms, whereas for the three-body term $\mathscr{V}^{(3)}(R, r, \theta)$, the coordinate r is the H_2^+ separation $r_{H_2^+}$, R is the distance between He and the center of mass of the diatomic, and θ is the angle between the two distance vectors $\vec{r}$ and $\vec{R}$. $\mathscr{V}^{(1)}$ corresponds to the respective atomic energies. The energies $\mathscr{V}_i^{(1)}$ and $\mathscr{V}_i^{(2)}$ were also determined at the respective level of theory from electronic structure calculations, and the contributions $\mathscr{V}_i^{(2)}$ were fitted to analytical expressions described in (19). The fitting parameters for the FCI and MRCI levels of theory were published before, and those for the MP2 level of theory are provided in the Supplementary Materials. Combining all this information, the three-body contribution $\mathscr{V}^{(3)}(R, r, \theta)$ was obtained on the grid used in the electronic structure calculations for $\mathscr{V}(R, r, \theta)$ and represented as a RKHS.

Scattering calculations

Integral scattering cross sections and scattering wave functions for $He − H_2^+$, resulting from a spatially distributed input wave packet, were evaluated using a home-written coupled-channel collision simulation based on the renormalized Numerov method (37, 38). Details on these calculations have been given in earlier work (26), and only the salient features are presented here. The wave packet simulations use Jacobi coordinates with $\vec{r}$ the vector between the hydrogen atoms,

$\vec{R}$ the vector from the dihydrogen center of mass to the helium atom, and θ the angle between the two vectors. With $R = |\vec{R}|$ and $r = |\vec{r}|$, the total Hamiltonian is then

$$H_{tot} = -\frac{\hbar^2}{2\mu_{cmplx}}\nabla^2_{\vec{R}} - \frac{\hbar^2}{2\mu_{diat}}\nabla^2_{\vec{r}} + V(R, r, \theta) \qquad (2)$$

where μ_{cmplx} is the reduced mass of the three-body complex, μ_{diat} is the reduced mass of the dihydrogen molecule, and $V(R, r, \theta)$ is the 3D PES. The total wave function of the system $\Psi(\vec{R}, \vec{r})$ is written as a product of R-, r-, and angularly dependent terms

$$\Psi^{JMvj\ell}(\vec{R}, \vec{r}) \propto \sum_{v'j'\ell'} G^{Jvj\ell}_{v'j'\ell'}(R)\chi_{diat,v'j'}(r) \sum_{m_j=-j}^{j}$$
$$\sum_{m_\ell=-\ell}^{\ell} C^{JM}_{m_j m_\ell} Y_{\ell,m_\ell}(\theta_R, \varphi_R) Y_{j,m_j}(\theta_r, \varphi_r) \qquad (3)$$

see (26) for more details. Channels consist of tuples of quantum numbers v, j, and ℓ, corresponding to diatomic vibration, rotation, and orbital angular momentum, respectively. In Eq. 3, $\chi_{diat,v,j}(r)$ designates the rovibrational eigenstates of the molecule. Starting from a given entrance channel, the Schrödinger equation is solved numerically to obtain the radial wave functions $G(R)$ for the exit channel with quantum numbers (v', j', ℓ') connected with the entrance channel (v, j, ℓ). The total angular momentum, $\vec{J}_{tot} = \vec{j} + \vec{L}$, obtained from coupling diatomic and orbital rotation, and parity are conserved under the Hamiltonian (2).

In the experiments, the $He − H_2^+$ complex (plus a leaving electron) is formed by Penning ionization ($He^* + H_2$), and the scattering calculations considered in the present work describe the half-collision on the $He − H_2^+$ PES. The initial wave packet $\phi(R)$ along the R-coordinate is approximated by Gaussian distributions centered around $R \approx 8$ a_0 (26). The experiment prepares the input wave packet with $j_{wp} = 0,1$ for para- and ortho-H_2^+, respectively. However, as the system is prepared in a superposition of J-states, individual simulations need to be carried out for each possible value of J and partial wave ℓ. Then, the integral cross section is calculated as a weighted sum over the individual contributions for a given collision energy $E_{col}/k_B \approx 2.5$ K. The J-weights, which were calculated separately (39), are shown in fig. S22. Experimentally, the initial state is prepared "in situ" whereby Penning ionization generates the $He − H_2^+$ complex. Thus, the initial state of the present quantum wave packet simulations is in fact the result of an incoherent decay of a population of He^*–H_2 complexes which leaves one with an unknown normalization. The experimentally observed quantity is a probability distribution $P(E)$ which is dimensionless. Here, the computed intensities are scaled such as to best reproduce the experimentally measured ones.

Evaluation of the collision cross section due to the spatially distributed input wave packet can be accomplished by expanding $\phi(R)$ in a basis of eigenfunctions of H_{tot}. To this end, the time-independent Schrödinger equation was solved on a discretized interval of 1002 energies ranging from 100 cm^{-1} below to 100 cm^{-1} above the dissociation threshold of the given entrance channel. Because full coupled-channel calculations are computationally demanding, the considered set of

initial wave packet quantum numbers J and ℓ was limited to $(\ell/J) \in$ $\{(0/0), (1/1), (2/2), (3/3), (4/4)\}$ for para- and $(\ell/J) \in \{(0/1), (1/1,2), (2/1,2,3), (3/2,3,4), (4/3,4,5)\}$ for ortho-dihydrogen, respectively. For each coupled channel calculation, a converged basis set of diatomic rotational states up to $j_{\max} = 19$ and diatomic vibrational states up to $v_{\max} = 5$ was used.

Solving the Schrödinger equation in this fashion allows for calculating the channel-resolved integral cross section for each energy in the discretized interval. For a given output channel, the eigenenergy $E_{v'j'\ell'} = E_{\mathrm{int},v'j'\ell'} + E_{\mathrm{kin},v',j',\ell'}$ can be decomposed into its internal and kinetic parts, respectively. By generating a histogram for all output channels (v',j',ℓ'), the cross section can be expressed as a function of kinetic energy, which can be compared with the experimental results. Next, the kinetic energy histogram is convoluted using a Gaussian envelope to account for the finite resolution in the experiments (26). Before convolution, and as shown in fig. S23, the computed peaks are sharp in E_{kin}, which is a signature of Feshbach resonances. It should be noted that experimental peaks are clearly distinguishable and energetically match the theoretical predictions. However, the peak shapes and heights can vary, dependent on the histogram resolution and convolution width. In this work, only single initial vibrational excitations ($v = 1$) were considered, to exploit the experimental resolution of separate j' peaks in the cross section as a function of kinetic energy (40). The final j' distributions $P(j')$ for the unmorphed and M2-morphed PESs are reported in fig. S24.

Morphing

The morphing transformation considered here is

$$V_{\mathrm{morphed}}(R, r, \theta) = \varepsilon V_{\mathrm{ab-initio}}(\alpha R, \beta r, \theta) \qquad (4)$$

In Eq. 4, the three parameters $(\alpha, \beta, \varepsilon)$ are used for energy (ε)– and geometry (α, β)–related scalings. For the purpose of this work, the angle θ was not modified. The morphing procedure described further below optimizes the values of $(\alpha, \beta, \varepsilon)$ such that the difference between observed and computed features of the resonances is minimized. Application of such a procedure modifies local features (e.g., slope and curvature) of the PES but maintains its global shape.

For morphing M1 and M2, the refinement with respect to experimental values is formulated as an optimization problem with a loss function

$$\mathscr{L} = \min_{\alpha, \beta, \varepsilon} \left[w_E \sum_{j'} |E_{\exp}^{(j')} - E_{\mathrm{calc}}^{(j')}(\alpha, \beta, \varepsilon)| + w_h \sum_{j'} \delta_{h(j')}^{\kappa} \right] \qquad (5)$$

to be minimized. Here, $E^{(j')}$ is the kinetic energy of each cross section corresponding to an exit channel j', and $\delta_{h(j')}^{\kappa}$ accounts for the difference in the peak heights between experimental and calculated values

$$\delta_{h(j')}^{\kappa} = \begin{cases} (\Delta h(j') - h_{\mathrm{noise}})^{\kappa}, & (\Delta h(j') - h_{\mathrm{noise}})^{\kappa} > 0, \\ 0, & (\Delta h(j') - h_{\mathrm{noise}})^{\kappa} \leq 0 \end{cases} \qquad (6)$$

where, $\delta_h(j')$ is regularized by subtracting $h_{\mathrm{noise}} = 10.0$ to avoid fitting experimental noise. By design, only values $\delta_h(j') > 0$ contribute to the error. Here, $\Delta h(j') = |h_{\exp}^{(j')} - \gamma h_{\mathrm{calc}}^{(j')}(\alpha, \beta, \varepsilon)|$, where $h^{(j')}$ is the peak height of the cross section corresponding to an exit channel j'. The parameter γ is recalculated after each iteration to best match the experiment by performing an additional 1d minimization over the squared difference in peaks heights. The weights $w_E = 1 \ (\mathrm{cm}^{-1})^{-1}$ and $w_h = 1$ ensure that all terms and the total loss $\mathscr{L}$ in Eq. 5 are dimensionless and can be used to bias the fit to better reproducing certain observables than others, which was, however, not done here.

The workflow to perform the optimization of Eq. 5 is shown schematically in Fig. 1. In the first step, ab initio points of the PES are used to generate a RKHS kernel. Depending on the morphing procedure chosen, a new RKHS needs to be generated (for M1) or the existing kernel will be reused (for M2). All kernels are constructed and evaluated using the "fast" method (34). The obtained PES is passed to the scattering code to perform the wave packet propagation. Next, the resulting cross sections are processed and then compared with the available experimental data. If the difference between experimental and calculated values matches a given tolerance, the cycle finishes; otherwise, the PES is modified by three parameters as described in Eq. 4 following the chosen morphing approach. The values of the parameters α, β, and ε were obtained by a nonlinear optimization using the NLopt package (41). For further details about the optimization procedure, see the Supplementary Materials.

Supplementary Materials

This PDF file includes:
Supplementary Text
Figs. S1 to S32
Table S1
References

REFERENCES AND NOTES

1. D. J. Wales, Exploring energy landscapes. *Annu. Rev. Phys. Chem.* **69**, 401–425 (2018).
2. S. Käser, L. I. Vazquez-Salazar, M. Meuwly, K. Töpfer, Neural network potentials for chemistry: Concepts, applications and prospects. *Digit. Discov.* **2**, 28–58 (2023).
3. J. Liu, E. J. Salumbides, U. Hollenstein, J. C. Koelemeij, K. S. Eikema, W. Ubachs, F. Merkt, Determination of the ionization and dissociation energies of the hydrogen molecule. *J. Chem. Phys.* **130**, 174306 (2009).
4. M. S. Child, D. J. Nesbitt, RKR-based inversion of rotational progressions. *Chem. Phys. Lett.* **149**, 404–410 (1988).
5. D. J. Nesbitt, M. S. Child, D. C. Clary, Rydberg–Klein–Rees inversion of high resolution van der Waals infrared spectra: An intermolecular potential energy surface for Ar+ HF (*v*=1). *J. Chem. Phys.* **90**, 4855–4864 (1989).
6. D. J. Nesbitt, M. S. Child, Rotational-RKR inversion of intermolecular stretching potentials: Extension to linear hydrogen bonded complexes. *J. Chem. Phys.* **98**, 478–486 (1993).
7. L. Kurtz, H. Rabitz, R. de Vivie-Riedle, Optimal use of time-dependent probability density data to extract potential-energy surfaces. *Phys. Rev. A* **65**, 032514 (2002).
8. J. M. Bowman, B. Gazdy, A simple method to adjust potential energy surfaces: Application to HCO. *J. Chem. Phys.* **94**, 816–817 (1991).
9. B. Gazdy, J. M. Bowman, An adjusted global potential surface for HCN based on rigorous vibrational calculations. *J. Chem. Phys.* **95**, 6309–6316 (1991).
10. M. Meuwly, J. M. Hutson, Morphing ab initio potentials: A systematic study of Ne–HF. *J. Chem. Phys.* **110**, 8338–8347 (1999).
11. R. Ramakrishnan, P. O. Dral, M. Rupp, O. A. von Lilienfeld, Big data meets quantum chemistry approximations: The Δ-machine learning approach. *J. Chem. Theor. Comp.* **11**, 2087–2096 (2015).
12. J. S. Smith, B. T. Nebgen, R. Zubatyuk, N. Lubbers, C. Devereux, K. Barros, S. Tretiak, O. Isayev, A. E. Roitberg, Approaching coupled cluster accuracy with a general-purpose neural network potential through transfer learning. *Nat. Commun.* **10**, 2903 (2019).
13. S. Käser, M. Meuwly, Transfer-learned potential energy surfaces: Toward microsecond-scale molecular dynamics simulations in the gas phase at CCSD (T) quality. *J. Chem. Phys.* **158**, 214301 (2023).
14. S. Thaler, J. Zavadlav, Learning neural network potentials from experimental data via differentiable trajectory reweighting. *Nat. Commun.* **12**, 6884 (2021).
15. S. N. Yurchenko, L. Lodi, J. Tennyson, A. V. Stolyarov, Duo: A general program for calculating spectra of diatomic molecules. *Comput. Phys. Commun.* **202**, 262–275 (2016).

16. K. T. Lorenz, M. S. Westley, D. W. Chandler, Rotational state-to-state differential cross sections for the HCl–Ar collision system using velocity-mapped ion imaging. *Phys. Chem. Chem. Phys.* **2**, 481–494 (2000).

17. R. A. Vargas-Hernández, Y. Guan, D. H. Zhang, R. V. Krems, Bayesian optimization for the inverse scattering problem in quantum reaction dynamics. *New J. Phys.* **21**, 022001 (2019).

18. T. van Mourik, G. J. Harris, O. L. Polyansky, J. Tennyson, A. G. Császár, P. J. Knowles, Ab initio global potential, dipole, adiabatic, and relativistic correction surfaces for the HCN–HNC system. *J. Chem. Phys.* **115**, 3706–3718 (2001).

19. D. Koner, J. C. San Vicente Veliz, A. van der Avoird, M. Meuwly, Near dissociation states for $H_2^+ - $He on MRCI and FCI potential energy surfaces. *Phys. Chem. Chem. Phys.* **21**, 24976–24983 (2019).

20. J. M. Hutson, Intermolecular forces from the spectroscopy of van der waals molecules. *Annu. Rev. Phys. Chem.* **41**, 123–154 (1990).

21. S. Adhikari, M. Baer, N. Sathyamurthy, HeH_2^+: Structure and dynamics. *Int. Rev. Phys. Chem.* **41**, 49–93 (2022).

22. A. Carrington, D. I. Gammie, A. M. Shaw, S. M. Taylor, J. M. Hutson, Observation of a microwave spectrum of the long-range $He\cdots H_2^+$ complex. *Chem. Phys. Lett.* **260**, 395–405 (1996).

23. D. I. Gammie, J. C. Page, A. M. Shaw, Microwave and millimeter-wave spectrum of the $He\cdots H_2^+$ long-range complex. *J. Chem. Phys.* **116**, 6072–6078 (2002).

24. O. Asvany, S. Schlemmer, A. van der Avoird, T. Szidarovszky, A. G. Császár, Vibrational spectroscopy of H_2He^+ and D_2He^+. *J. Mol. Struct.* **377**, 111423 (2021).

25. D. Kedziera, G. Rauhut, A. G. Császár, Structure, energetics, and spectroscopy of the chromophores of HHe_n^+, $H_2He_n^+$, and He_n^+ clusters and their deuterated isotopologues. *Phys. Chem. Chem. Phys.* **24**, 12176–12195 (2022).

26. B. Margulis, K. P. Horn, D. M. Reich, M. Upadhyay, N. Kahn, A. Christianen, A. van der Avoird, G. C. Groenenboom, C. P. Koch, M. Meuwly, E. Narevicius, Tomography of Feshbach resonance states. *Science* **380**, 77–81 (2023).

27. C. Chin, R. Grimm, P. Julienne, E. Tiesinga, Feshbach resonances in ultracold gases. *Rev. Mod. Phys.* **82**, 1225–1286 (2010).

28. J. Pérez Ríos, *Introduction to Cold and Ultracold Chemistry: Atoms, Molecules, Ions and Rydbergs* (Springer, 2020).

29. R. J. Le Roy, J. M. Hutson, Improved potential energy surfaces for the interaction of H_2 with Ar, Kr, and Xe. *J. Chem. Phys.* **86**, 837–853 (1987).

30. D. Koner, M. Meuwly, Permutationally invariant, reproducing kernel-based potential energy surfaces for polyatomic molecules: From formaldehyde to acetone. *J. Chem. Theor. Comp.* **16**, 5474–5484 (2020).

31. S. Chmiela, V. Vassilev-Galindo, O. T. Unke, A. Kabylda, H. E. Sauceda, A. Tkatchenko, K.-R. Müller, Accurate global machine learning force fields for molecules with hundreds of atoms. *Sci. Adv.* **9**, eadf0873 (2023).

32. M. A. Nielsen, I. L. Chuang, *Quantum Computation and Quantum Information* (Cambridge Univ. Press, 2010).

33. P. J. Ollitrault, A. Miessen, I. Tavernelli, Molecular quantum dynamics: A quantum computing perspective. *Acc. Chem. Res.* **54**, 4229–4238 (2021).

34. O. T. Unke, M. Meuwly, Toolkit for the construction of reproducing kernel-based representations of data: Application to multidimensional potential energy surfaces. *J. Chem. Inf. Model.* **57**, 1923–1931 (2017).

35. T.-S. Ho, H. Rabitz, A general method for constructing multidimensional molecular potential energy surfaces from ab initio calculations. *J. Chem. Phys.* **104**, 2584–2597 (1996).

36. H.-J. Werner, P. J. Knowles, G. Knizia, F. R. Manby, M. Schütz, Molpro, version 2019.2, a package of ab initio programs (2019).

37. B. R. Johnson, The renormalized numerov method applied to calculating bound states of the coupled-channel schroedinger equation. *J. Chem. Phys.* **69**, 4678–4688 (1978).

38. F. X. Gadéa, H. Berriche, O. Roncero, P. Villarreal, G. Delgado Barrio, Nonradiative lifetimes for LiH in theA state using adiabatic and diabatic schemes. *J. Chem. Phys.* **107**, 10515–10522 (1997).

39. M. Pawlak, Y. Shagam, A. Klein, E. Narevicius, N. Moiseyev, Adiabatic variational theory for cold atom–molecule collisions: Application to a metastable helium atom colliding with *ortho-* and *para*-hydrogen molecules. *J. Phys. Chem. A* **121**, 2194–2198 (2017).

40. B. Margulis, J. Narevicius, E. Narevicius, Direct observation of a Feshbach resonance by coincidence detection of ions and electrons in penning ionization collisions. *Nat. Commun.* **11**, 3553 (2020).

41. S. G. Johnson, The nlopt nonlinear-optimization package, http://github.com/stevengj/nlopt. [accessed 15 October 2021].

42. D. De Fazio, M. de Castro-Vitores, A. Aguado, V. Aquilanti, S. Cavalli, The $He + H_2^+H_2^+ \rightarrow HeH^+ + H$ reaction: Ab initio studies of the potential energy surface, benchmark time-independent quantum dynamics in an extended energy range and comparison with experiments. *J. Chem. Phys.* **137**, 244306 (2012).

43. A. Aguado, M. Paniagua, A new functional form to obtain analytical potentials of triatomic molecules. *J. Chem. Phys.* **96**, 1265–1275 (1992).

44. M. F. Falcetta, P. E. Siska, The interaction between He and H_2^+: Anisotropy, bond length dependence and hydrogen bonding. *Mol. Phys.* **97**, 117–125 (1999).

45. D. M. Bishop, J. Pipin, Static electric properties of H and He. *Chem. Phys. Lett.* **236**, 15–18 (1995).

46. L. Velilla, B. Lepetit, A. Aguado, A. Beswick, M. Paniagua, The H_3^+ rovibrational spectrum revisited with a global electronic potential energy surface. *J. Chem. Phys.* **129**, 084307 (2008).

47. J. A. Coxon, P. G. Hajigeorgiou, Experimental Born–Oppenheimer potential for the $X^1\Sigma^+$ ground state of HeH^+: Comparison with the ab initio potential. *J. Mol. Struct.* **193**, 306–318 (1999).

48. R. J. Le Roy, *LEVEL 7.5: A Computer Program to Solve the Radial Schrödinger Equation for Bound and Quasibound Levels* (Waterloo, Ontario N2L 3G1, Canada, 2002).

49. A. Balakrishnan, V. Smith, B. Stoicheff, Dissociation energy of the hydrogen molecule. *Phys. Rev. Lett.* **68**, 2149–2152 (1992).

50. B. M. Dinelli, C. R. Le Sueur, J. Tennyson, R. D. Amos, Ab initio ro-vibrational levels of H_3^+ beyond the Born-Oppenheimer approximation. *Chem. Phys. Lett.* **232**, 295–300 (1995).

51. S. Soritz, D. Moser, H. Gruber-Wölfler, Comparison of derivative-free algorithms for their applicability in self-optimization of chemical processes. *Chem. Methods* **2**, e202100091 (2022).

52. T. H. Rowan, Functional stability analysis of numerical algorithms, thesis, The University of Texas at Austin (1990).